

## THE STELLAR INITIAL MASS FUNCTION IN EARLY-TYPE GALAXIES FROM ABSORPTION LINE SPECTROSCOPY. I. DATA AND EMPIRICAL TRENDS

PIETER G. VAN DOKKUM<sup>1</sup> & CHARLIE CONROY<sup>2,3</sup>

*Submitted to the Astrophysical Journal*

### ABSTRACT

The strength of gravity-sensitive absorption lines in the integrated light of old stellar populations is one of the few direct probes of the stellar initial mass function (IMF) outside of the Milky Way. Owing to the advent of fully depleted CCDs with little or no fringing it has recently become possible to obtain accurate measurements of these features. Here we present spectra covering the wavelength ranges  $0.35\ \mu\text{m} - 0.55\ \mu\text{m}$  and  $0.72\ \mu\text{m} - 1.03\ \mu\text{m}$  for the bulge of M31 and 34 early-type galaxies from the SAURON sample, obtained with the Low Resolution Imaging Spectrometer on Keck. The signal-to-noise ratio is  $\gtrsim 200\ \text{\AA}^{-1}$  out to  $1\ \mu\text{m}$ , which is sufficient to measure gravity-sensitive features for individual galaxies and to determine how they depend on other properties of the galaxies. Combining the new data with previously obtained spectra for globular clusters in M31 and the most massive elliptical galaxies in the Virgo cluster we find that the dwarf-sensitive Na I  $\lambda 8183, 8195$  doublet and the FeH  $\lambda 9916$  Wing-Ford band increase systematically with velocity dispersion, while the giant-sensitive Ca II  $\lambda 8498, 8542, 8662$  triplet decreases with dispersion. These trends are consistent with a varying IMF, such that galaxies with deeper potential wells have more dwarf-enriched mass functions. In a companion paper (Conroy & van Dokkum 2012) we use a comprehensive stellar population synthesis model to demonstrate that IMF effects can be separated from age and abundance variations and quantify the IMF variation among early-type galaxies.

*Keywords:* cosmology: observations — galaxies: evolution

### 1. INTRODUCTION

The form of the stellar initial mass function (IMF) is of fundamental importance for many areas of astrophysics and one of the largest uncertainties in the interpretation of the integrated light of stellar populations. The IMF is reasonably well constrained in the disk of the Milky Way as stars can be counted more or less directly. For the past decade the consensus has been that the Milky Way IMF is a powerlaw with a logarithmic slope of  $\sim 2.3$  at  $M \gtrsim 1 M_{\odot}$ , with a gradual turnover at lower masses (see, e.g., Kroupa 2001; Chabrier 2003). This turnover can be interpreted as a characteristic mass: in the Milky Way disk, the formation of stars with masses of a few tenths of the mass of the Sun is apparently favored over the formation of lower and higher mass stars. This departure from a powerlaw is important, as most of the stellar mass- and number density is in the form of low mass stars. As a result, apparently subtle changes in the form of the low mass IMF significantly alter the mass-to-light ( $M/L$ ) ratios of galaxies. As an example, for the same total luminosity, a Salpeter (1955) IMF with a constant slope of 2.3 down to  $M = 0.1 M_{\odot}$  implies a  $1.6\times$  higher stellar mass than a Chabrier (2003) IMF.

It seems likely that the IMF in other present-day spiral galaxies is similar to that in the Milky Way disk, but that does not mean that the IMF has the same form in all galaxies and at all epochs. In particular, the most massive elliptical galaxies have had very different star formation histories than spiral galaxies. Their central regions are thought to have formed in short-lived, highly dissipative events at high redshift (e.g., Naab et al. 2007; Hopkins et al. 2009; Kormendy et al. 2009;

van Dokkum et al. 2010; Oser et al. 2010). Densities, temperatures, turbulent velocities, and the dust and metal content were almost certainly different from conditions in the present-day Milky Way, which may well have led to a different characteristic stellar mass (e.g., Padoan & Nordlund 2002; Bate, Bonnell, & Bromm 2003; Larson 2005; Krumholz 2011; Myers et al. 2011).

Motivated by these and other arguments, several recent studies have attempted to observationally measure or constrain the form of the IMF in elliptical galaxies or their progenitors. In 2008, several papers argued that the IMF may have been “bottom-light” (dwarf-deficient) at early times, with a higher characteristic mass than the Milky Way IMF. van Dokkum (2008) [vD08] used the ratio of luminosity evolution to color evolution of massive galaxies in clusters to constrain the IMF, a test first proposed by Tinsley (1980). Davé (2008) found that the specific star formation rates of galaxies at  $z \sim 2$  are difficult to explain in the context of galaxy formation models unless the characteristic mass was higher than today. Wilkins, Trentham, & Hopkins (2008), following Fardal et al. (2007), argued that the  $z = 0$  stellar mass density is lower than the integral of the cosmic star formation history, unless star formation estimates at high redshift overestimate the formation rate of low mass stars.

Short of counting individual stars, the most direct way to constrain the low mass IMF is to detect and quantify the light emitted by dwarf stars. As has been known for a long time, this is possible thanks to gravity-sensitive absorption features whose strengths are different in dwarfs and giants (see, e.g., Spinrad 1962; Cohen 1978; Carter, Visvanathan, & Pickles 1986; Couture & Hardy 1993; Conroy & van Dokkum 2012). The strongest dwarf-sensitive features are the Na I  $\lambda 8183, 8195$  doublet (e.g., Faber & French 1980; Schiavon et al. 1997a) and the FeH  $\lambda 9916$  Wing-Ford band (e.g., Wing & Ford 1969; Schiavon, Barbuy, & Singh 1997b);

<sup>1</sup> Department of Astronomy, Yale University, New Haven, CT, USA

<sup>2</sup> Department of Astronomy & Astrophysics, University of California, Santa Cruz, CA, USA

<sup>3</sup> Harvard-Smithsonian Center for Astrophysics, Cambridge, MA, USA

the strongest giant-sensitive feature (in the optical) is the Ca II  $\lambda 8498, 8542, 8662$  triplet (e.g., Cenarro et al. 2003). This work is technically challenging as dwarfs contribute only 5% – 10% of the integrated light of stellar populations. Therefore, a 30% absorption feature in the spectra of dwarf stars has a depth of only a few percent in integrated light. Detecting IMF variations therefore requires line measurements with exquisite accuracy ( $\lesssim 0.3\%$ ) in spectral regions that are plagued by strong sky emission and (typically) poor detector performance.

Owing to the advent of fully depleted, high resistivity CCDs it has recently become possible to measure absorption lines in the far red with the required accuracy to detect variations in the dwarf-to-giant ratio. Using the upgraded red arm of the Low Resolution Imaging Spectrograph on Keck (LRIS; Oke et al. 1995; Rockosi et al. 2010) we found that massive elliptical galaxies in the Virgo and Coma clusters have enhanced Na I and Wing-Ford band absorption compared to metal-rich globular clusters and to expectations from stellar population synthesis models, indicating that the IMF in these galaxies is “bottom-heavy” with respect to that of the Milky Way (van Dokkum & Conroy 2010, 2011; Conroy & van Dokkum 2012). This result is consistent with constraints on the masses of early-type galaxies as derived from stellar dynamics and lensing (e.g., Treu et al. 2010; Auger et al. 2010; Spiniello et al. 2011; Thomas et al. 2011; Dutton, Mendel, & Simard 2012; Spiniello et al. 2012; Cappellari et al. 2012). However, it is opposite to the conclusions from the 2008 studies.

The main uncertainties in our initial study (van Dokkum & Conroy 2010) are the small sample size (four galaxies in Virgo with Na I and Wing-Ford measurements and four galaxies in Coma with Na I measurements), the relatively low signal-to-noise ratio (S/N) of the spectra, and the fact that our modeling did not allow for abundance variations of individual elements. As discussed in detail in Conroy & van Dokkum (2012) abundance variations can be separated from IMF variations by analyzing different absorption lines of the same element. As an example, the Wing-Ford band depends on the IMF but also on  $[\text{Fe}/\text{H}]$ , and by comparing the strength of the Wing-Ford band to other iron lines the two variables can be separated. This approach requires high quality data and a stellar population synthesis model that allows simultaneous fitting of individual elemental abundances, the IMF, and other stellar population parameters.

In the present paper we describe newly obtained high S/N Keck spectroscopy of 34 early-type galaxies spanning a large range in velocity dispersion and abundance patterns. We show that dwarf- and giant-sensitive absorption lines can be measured accurately for individual galaxies, and compare the measurements to the most massive Virgo ellipticals and to M31 globular clusters. In an Appendix we re-assess the results of vD08 in the context of recent results by van der Wel et al. (2008) and Holden et al. (2010), as well as the Conroy & van Dokkum (2012) stellar population synthesis models. In a companion paper (Conroy & van Dokkum 2012b [paper II]) we fit the new Keck spectra with the stellar population synthesis model of Conroy & van Dokkum (2012) to quantify the IMF variation.

## 2. SAMPLE AND OBSERVATIONS

### 2.1. Sample Selection

The primary sample comprises a subset of the early-type galaxies observed in the SAURON survey (Bacon et al. 2001; de Zeeuw et al. 2002). Specifically, we observed 34 of the 48 E/S0 galaxies listed in Table 1 of Kuntschner et al. (2010). As discussed in de Zeeuw et al. (2002) the SAURON parent sample is not complete but was selected to span a large range in ellipticity and absolute magnitude. We could not observe the entire Kuntschner et al. (2010) sample because of visibility constraints and the fact that we only had a single night of LRIS time. The 14 galaxies that were excluded are NGC 3032, NGC 3156, NGC 3489, NGC 4150, NGC 4526, NGC 4550, and NGC 5831, because we gave preference to galaxies with ages  $\geq 9$  Gyr; NGC 4374, NGC 4387, NGC 4477, and NGC 5198, as we gave preference to galaxies with metallicity  $0.05 < Z < 0.20$  and  $\alpha$ -enhancement  $0.15 < [\alpha/\text{Fe}] < 0.25$  in that same part of the sky; and NGC 5982, NGC 7332, and NGC 7457, as they were not observable in January.

The sample is compared to the SAURON parent sample in Fig. 1. The LRIS sample discussed in this paper comprises most of the SAURON sample, with an intentional bias against the youngest galaxies (which tend to be fast rotators with low dispersions and low  $\alpha$ -enhancements). Using the derived quantities of Kuntschner et al. (2010) for  $r < r_e/8$ , the galaxies in the LRIS sample have a median age of 11.2 Gyr, a median metallicity  $[Z/H]$  of 0.08, and a median  $\alpha$ -enhancement of 0.24. It contains 7 slow rotators and 27 fast rotators, as defined by Emsellem et al. (2007).

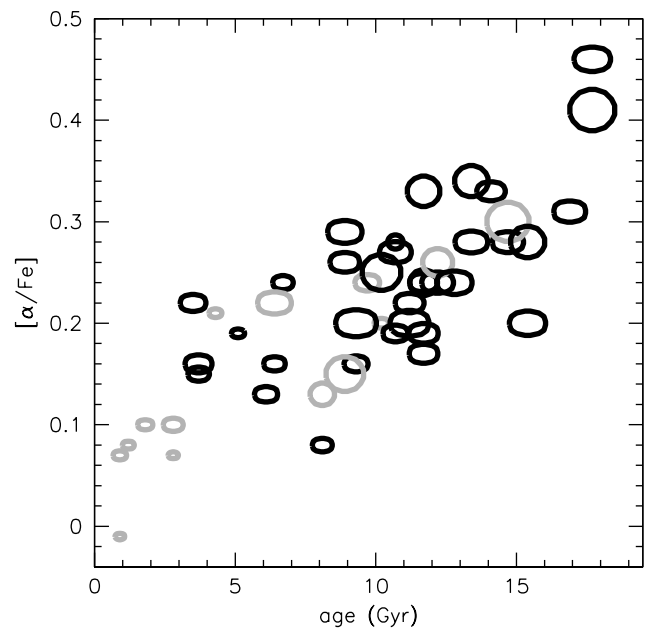


**Figure 1.** Sample selection. The points show the full SAURON sample of Kuntschner et al. (2010) in the plane of  $\alpha$ -enhancement versus age within  $r_e/8$ . The symbol size scales with the velocity dispersion. Circles denote slow rotators and ellipses denote fast rotators. Black points were observed with LRIS; grey points (mostly young galaxies with low velocity dispersions) were not observed.

In addition to the SAURON galaxies we observed the central regions of the bulge of M31. M31 has played an important if somewhat confusing role in the decades-long quest to constrain the low mass end of the IMF through absorption line spectroscopy. Spinrad & Taylor (1971) and Faber & French

(1980) suggested that the nuclear regions have a very large population of low mass stars, largely based on anomalously strong Na I  $\lambda$ 8183,8195 absorption. However, other studies have shown that the effects of metallicity complicate the interpretation (e.g., Cohen 1978; Carter et al. 1986).

## 2.2. Observing Strategy

The galaxies were observed on the night of January 21, 2012 with LRIS on the Keck I telescope. The 680 nm dichroic was used to split the light into the blue and red arms. In the blue arm the  $6001\text{mm}^{-1}$  grism, blazed at  $4000\text{\AA}$ , gave a spectral coverage of  $3000\text{\AA} - 5600\text{\AA}$ . In the red arm the  $6001\text{mm}^{-1}$  grating blazed at  $10,000\text{\AA}$  was set to cover the wavelength range  $7100\text{\AA} - 10,400\text{\AA}$ . We used a relatively narrow ( $0''.7$ ) slit to maximize the spectral resolution. This is not important for resolving lines in the galaxy spectra as they all have  $\sigma \gtrsim 100\text{ km s}^{-1}$ , but very helpful when correcting for sky emission and absorption. The spectral resolution  $\sigma_{\text{instr}}$ , as measured from sky emission lines, is  $\approx 60\text{ km s}^{-1}$  in the blue arm (at  $5500\text{\AA}$ ) and ranges from  $\approx 65\text{ km s}^{-1}$  at  $7200\text{\AA}$  to  $\approx 45\text{ km s}^{-1}$  at  $9500\text{\AA}$  in the red arm. The red detector was binned by a factor two in the spatial direction to reduce read-out time. After applying the same binning (in software) to the data from the blue detector the pixel scales are identical at  $0''.27$ .

Each galaxy was observed for 540 s, split into three 180 s exposures. The telescope was moved along the slit between exposures, such that each galaxy was observed in two positions on one of the two detectors and in one position on the other detector. The slit was always positioned along the minor axis of the galaxy to minimize galaxy light near the edges of the slit and facilitate sky subtraction. The white dwarf GD 153 (see Bohlin 1996) was observed to correct for the wavelength variation in the detector and instrument response. At the beginning and end of the night arc lamp exposures were obtained for wavelength calibration. Conditions were clear; we note that our initial data for this project (van Dokkum & Conroy 2010) were taken through clouds and therefore had significantly lower S/N ratio than the data described here.

## 3. DATA REDUCTION

### 3.1. Overview

Although the LRIS long slit has a length of  $168''$  the effective slit length is much shorter. The reason is that the LRIS blue and red CCDs are both mosaics, and the slit is projected onto two independent detectors. On the blue side,  $75''$  is imaged on one detector,  $14''$  falls in a gap between two detectors, and  $79''$  falls on another detector. The detectors have slightly different characteristics, and due to optical distortions and flexure the relation between pixel location and wavelength needs to be determined independently for each  $\sim$  half of the slit. As the flexure varies with the position of the telescope, each 540 s sequence effectively comprises 12 independent exposures: 2 detectors  $\times$  2 arms  $\times$  3 dither positions. Another consequence of the somewhat peculiar slit geometry is that the galaxies often extend to the edges of the slit halves, complicating the sky subtraction.

Within these constraints the data reduction followed fairly standard procedures: bias subtraction, using the overscan regions; correction for s-distortion; wavelength calibration, using a combination of arc lamps and the location of sky emission lines; subtraction of a 2D model of the sky lines; cosmic

ray identification and combination of the individual science exposures in a sequence; extraction of one-dimensional spectra, mimicking a circular aperture of  $r = r_e/8$ ; correction for detector and instrument response; and correction for atmospheric absorption. This last step is one of the most critical, as a near-perfect correction is required for our purposes. The steps are detailed below. The red and blue spectra were treated in the same way, unless noted otherwise.

### 3.2. Distortion Correction and Wavelength Calibration

After bias subtraction the spectra were placed on an undistorted output grid that is linear in the wavelength and spatial axes. The s-distortion was mapped by fitting the position of the galaxy in the spatial direction with a Gaussian at 50-pixel intervals, and then fitting a 3<sup>d</sup>-order polynomial to the measured positions. A two-dimensional wavelength solution was obtained from arc lamp exposures, by fitting 3<sup>d</sup>-order polynomials in the wavelength direction and the spatial direction. The median residual is typically  $\approx 0.2\text{\AA}$ ; higher order polynomials did not improve the fit. These arc lamp solution capture the tilt of the sky lines and the distortion in the wavelength direction, but flexure in the spectrograph causes offsets of typically  $\approx 2\text{\AA}$  between the science exposures and arc lamps. Bright sky emission lines were used to find the zero-order correction for these differences between the arc lamps and the science exposures. A small linear correction was applied after extraction of the spectra (see § 3.7).

The spectra were mapped onto an output grid with  $1\text{\AA}$  pixels in the wavelength direction and  $0''.27$  pixels in the spatial direction, using linear interpolation. This resampling method mostly conserves the noise properties of the data and the sharp edges of cosmic rays, and does not introduce significant aliasing in sky lines which would complicate their subtraction.

### 3.3. Sky Subtraction

The subtraction of sky emission lines is complicated by the fact that the galaxies cover a substantial fraction of the slit. Sky lines were subtracted from the 2D spectra in several steps, making use of the fact that each of the two detectors has at least one exposure in each sequence with negligible galaxy light (see § 2.2). First, a 1D model of the sky was created using these sky exposures, by median filtering in the spatial direction. Next, the spatial variation in the sky exposures was modeled using a low order polynomial. A 2D sky model for each detector was generated by replicating the 1D model in the spatial direction, weighted by the polynomial fit. This (nearly) noise-free model of the sky emission for each detector was then subtracted from the galaxy exposures.

This procedure is effective in removing sky emission without affecting the galaxy light. However, residuals remain, due to the variation in the intensity of sky lines on timescales of a few minutes: the sky exposure is typically about 4 minutes removed in time from the galaxy exposures on the same detector. These sky line residuals were removed by subtracting the average of the two edges of the detector at each wavelength. This step reduces the variation in the sky lines to the photon noise for most galaxies, but it comes at a cost. For the largest galaxies there is still detectable galaxy light at the edge of the slit, and by subtracting this light we reduced the utility of the data for measuring gradients in absorption features. Furthermore, if the gradients are strong the subtraction alters the observed absorption line strengths. The maximum effect on absorption lines occurs when the gradient is such

that the absorption feature vanishes at the edge of the slit. In that case, the observed absorption at radius  $r$  will be increased by a factor of  $F_{\text{edge}}/F_r$ , with  $F_{\text{edge}}$  the (subtracted) galaxy flux at the edge of the slit and  $F_r$  the galaxy flux at radius  $r$ . The galaxy flux at the edge is always  $\ll 1\%$  of the average flux in our extraction aperture; this effect is therefore negligible in our analysis.

### 3.4. Cosmic Ray Identification and Combination of Exposures

Cosmic rays and other defects were identified in the following way. First, a model for the galaxy light was created by taking the median of the three individual exposures and then median filtering in the spatial direction. After subtraction of this model, residual galaxy light was removed by fitting and subtracting a 7<sup>th</sup>-order polynomial in the spatial direction. The resulting residual exposure contains noise and cosmic rays. Next, a 2D-model of the total flux in each exposure was created from the 2D sky model and the galaxy model. This total flux model  $M$  was converted to a noise model  $N$  through  $N = g^{-1} \sqrt{M} \times \bar{g}$ , with  $g$  the gain. A pixel was flagged as a cosmic ray when its flux in the residual exposure was  $7\times$  higher than the flux in the noise model. Due to the linear resampling cosmic rays are slightly smoothed with respect to the original exposures; to take this into account all pixels neighboring cosmic ray pixels were also flagged.

The three exposures of each galaxy were summed to create a combined, sky subtracted 2D output frame. Pixels affected by a cosmic ray in one exposure were replaced by  $1.5\times$  the sum of the other two exposures. In the rare cases where two exposures were affected by a cosmic ray the pixel in the output frame is  $3\times$  the flux in the unaffected exposure. The locations of pixels that were affected by a cosmic ray in at least one of the three exposures are stored for diagnostic purposes.

### 3.5. Extraction of Spectra and Flux Calibration

One-dimensional spectra were extracted from the 2D spectra by summing the flux in the spatial direction. An extraction aperture of  $r_e/8$  was used; the effective radii were taken from Kuntschner et al. (2010) and corrected to the minor axis. This aperture is also used by the SAURON survey (along with larger apertures), allowing direct comparisons to their results. A “straight” summation of the long slit spectrum over the range  $-r_e/8 < r < r_e/8$  would be weighted more towards the center of the galaxy than the summation in a circular aperture of SAURON. To mimic summation in a circular aperture with radius  $r = r_e/8$  we extracted the spectrum as follows:

$$F_\lambda = \sum_{y=-1}^1 F_{\lambda,y} + \sum_{y=-n}^{-2} -y F_{\lambda,y} + \sum_{y=2}^n y F_{\lambda,y}, \quad (1)$$

with  $y$  the pixel coordinate in the spatial direction (with the galaxy centered in the middle of pixel zero) and  $n$  the nearest integer number of pixels corresponding to  $r_e/8$ . The first term in Eq. 1 is a straightforward sum of the central three rows, corresponding to a rectangular aperture of  $0''.81 \times 0''.70$ . The other two terms extend the summation to  $r_e/8$ , weighting by the distance from the central row. Weighted in this manner the spectra can be compared directly to the SAURON measurements, and represent a larger fraction of the galaxy light. For an  $r^{1/4}$  law, a circular aperture of  $r_e/8$  contains  $\sim 10\%$  of a galaxy’s total flux.

Next, the extracted spectra were calibrated using a response curve that produces a flat spectrum for an object with constant  $F_\lambda$ . No absolute calibration was attempted, but given the rapid fall-off of the detector response at wavelengths  $\gtrsim 9600 \text{ \AA}$  it is important to obtain a reasonably accurate relative calibration as a function of wavelength. The response curve was created as follows. First, a boxcar-smoothed high S/N ratio halogen lamp spectrum was used to model the small-scale variations in the response. This spectrum is shown by the dashed line in Fig. 2. Next, the extracted spectrum (corrected for atmospheric absorption; see below) of the white dwarf GD 153 was divided by the halogen-derived response curve and then divided by the Rayleigh-Jeans approximation of its spectrum ( $F_\lambda \propto \lambda^{-4}$ ). The residual spectrum was fitted by a low order polynomial. The final response curve, indicated by the solid line in Fig. 2, was created by multiplying this polynomial by the halogen-derived response curve. From a comparison of the galaxy spectra to the stellar population synthesis models of paper II we estimate that the relative uncertainty in the calibration as a function of wavelength is  $\lesssim 5\%$  on  $\sim 1000 \text{ \AA}$  scales.

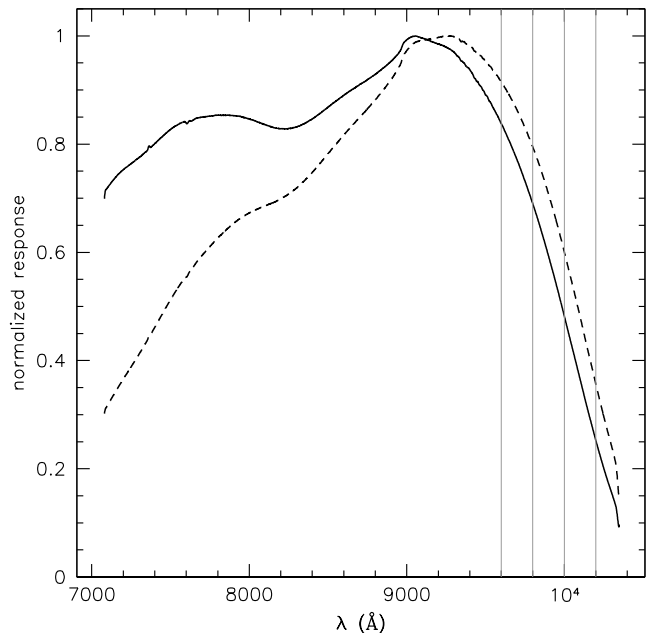


**Figure 2.** Response curve that was used to calibrate the red spectra (solid line), as determined from the white dwarf GD 153. Division by the response curve produces a flat spectrum for an object with constant  $F_\lambda$ . The dashed line shows a high S/N halogen lamp spectrum which was used to capture the small-scale variation in the response.

### 3.6. Correction for Atmospheric Absorption

As we aim to measure weak stellar absorption lines with high accuracy it is crucial to correct for absorption in our own atmosphere. The strongest atmospheric absorption features in the optical are the “A” and “B” bands of  $\text{O}_2$  at  $\sim 6870 \text{ \AA}$  and  $\sim 7600 \text{ \AA}$  respectively. However, the weaker but numerous  $\text{H}_2\text{O}$  bands in the regions  $8100 \text{ \AA} - 8400 \text{ \AA}$  and  $8900 \text{ \AA} - 9800 \text{ \AA}$  are a more serious challenge for our program, as several key features (in particular the Na I doublet) fall in this wavelength region.

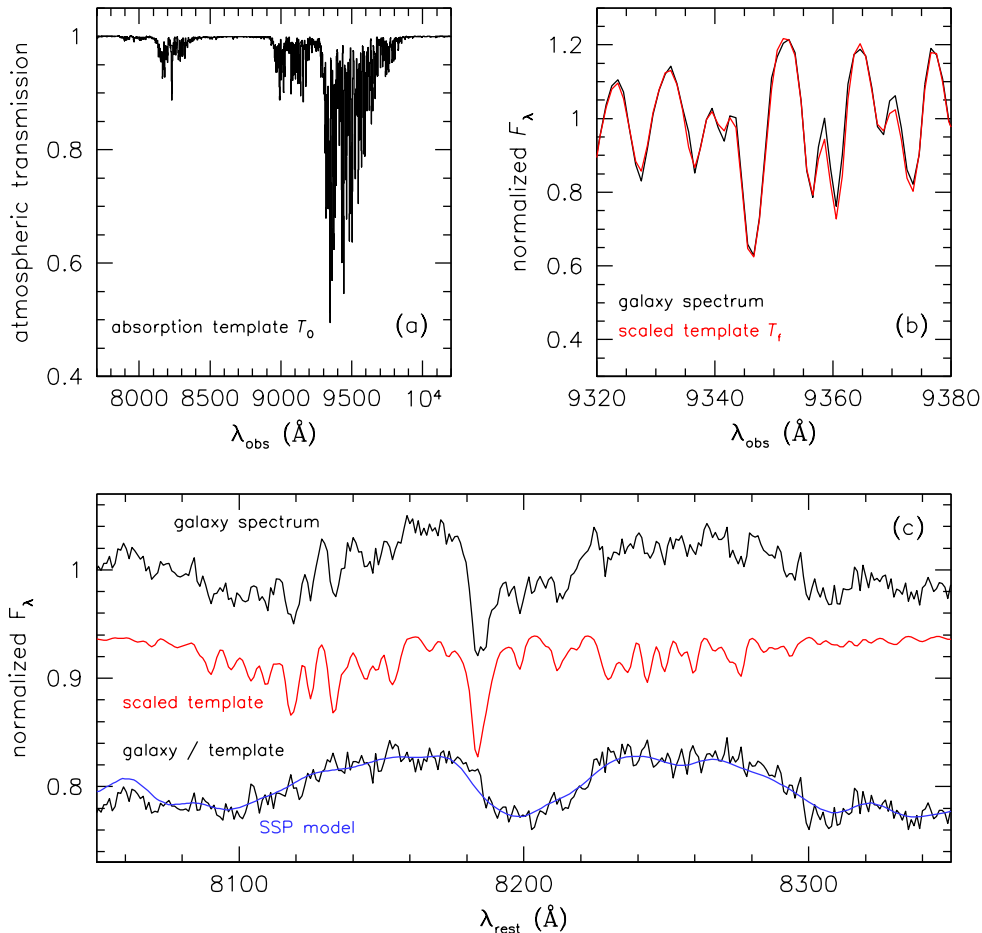


**Figure 3.** Illustration of our correction for atmospheric absorption, for NGC 5846. (a) Template atmospheric absorption spectrum. (b) Galaxy spectrum (black) and template absorption spectrum (red) in the  $\sim 9350 \text{ \AA}$  region, where the absorption is strong. The template is scaled to match the observed galaxy spectrum in this wavelength region. (c) Galaxy spectrum before and after division by the scaled absorption template, near the Na I doublet. The blue line shows the best-fitting stellar population synthesis model from paper II.

The standard method to correct for atmospheric absorption is to observe blue stars that are located near the science targets in the sky. Typically a star is observed before and after the target, so that the varying absorption can be interpolated to match the time and sky position of the science observation (see, e.g., Kriek et al. 2008). In practice telluric standards are usually A stars, as O and B stars are rare and typically not available in the general direction of the science target. This procedure suffers from several drawbacks. A stars have strong Paschen lines at wavelengths  $> 8200 \text{ \AA}$ , which need to be divided out before the spectrum can be used to model the atmospheric absorption. They also have weak metal lines which can introduce systematic errors at the 0.5% – 1% level. Finally, telluric standards carry significant overhead, particularly given the requirement that they are observed before and after each science target.

Here we take a different approach, and correct for atmospheric absorption by scaling a template spectrum to the observed absorption. The scaling is parameterized by

$$T_f = 1 + f(T_0 - 1), \quad (2)$$

with  $f$  a scale factor and  $T_0$  a template absorption spectrum. For each galaxy the best-fitting value of  $f$  is found by minimizing  $|G - T_f|$ , with  $G$  the galaxy spectrum. The fit is done

over the wavelength range  $9320 \text{ \AA} - 9380 \text{ \AA}$ , as this region is dominated by strong atmospheric  $\text{H}_2\text{O}$  lines and does not contain strong (redshifted) galaxy absorption features. Prior to the minimization  $G$  and  $T_f$  are divided by a 4<sup>th</sup>-order polynomial fit in the wavelength range  $9250 \text{ \AA} - 9650 \text{ \AA}$ . The template  $T_0$  is appropriate for Mauna Kea and smoothed to the instrumental resolution.

The procedure (also explored in Schiavon 1998) is illustrated in Fig. 3 for one of the sample galaxies (NGC 5846). The theoretical absorption template is shown in panel (a). Panel (b) shows the detailed region of the template around the strongest absorption lines, where the fit is done to determine the best match to the galaxy spectrum. The top spectrum in panel (c) shows the significant effect of atmospheric absorption lines on the region around the Na I  $\lambda 8183, 8195$  feature. After division by the scaled template (red) the narrow sky lines are nearly perfectly removed. The blue line is the best-fitting template from paper II. An analysis of the residuals of these fits in regions affected by sky absorption shows that the absorption correction is good to about 5 – 10% of the feature strength. At our spectral resolution the strongest absorption feature in the  $8000 \text{ \AA} - 8500 \text{ \AA}$  range is  $\sim 10\%$ , which implies that the largest residuals are 0.5 – 1%. As the width of sky absorption lines is typically  $\sim 20\%$  of the width of galaxy

absorption features, this results in a 0.1–0.2% uncertainty in the strength of a galaxy absorption line that coincides with a relatively strong sky absorption line.

### 3.7. Optimizing the Wavelength Calibration

The standard wavelength calibration as described in § 3.2 is correct to approximately  $\pm 1$  pixel ( $\pm 30$  km s<sup>-1</sup>) over the entire wavelength range. Although this level of accuracy is sufficient for most purposes, it is a source of uncertainty in the analysis in paper II. The reason for this sensitivity to the wavelength calibration is that in our methodology a template spectrum is directly fit to the observed spectrum. As a result, a small error in the wavelength calibration increases the  $\chi^2$  value of the fit. In the fitting this increase can be partially compensated by changing the line strength in the model, thus potentially leading to erroneous abundances and other fit parameters.

We optimized the wavelength calibration by fitting an  $\alpha$ -enhanced, 13.5 Gyr old stellar population synthesis model to the blue and red spectra in narrow wavelength regions. The spectra were divided in  $\sim 20$  regions, each with a width of 250 Å. The model was smoothed to the velocity dispersion of the galaxies and fit to each of the regions, with velocity as the only free parameter. The deviations from the average velocity, expressed in Å, were fit with a linear function in wavelength. Each galaxy was fit separately, and the red and blue spectra were treated independently. The linear fits to the corrections were then applied to the wavelengths of the extracted spectra. The fit procedure is illustrated in Fig. 4, for four galaxies that exhibit the full range of corrections. The slope of the required corrections broadly correlates with the time of night (and hence with the NGC number of the galaxies), presumably because the true wavelength calibration deviates more and more from the arc lamp solution. After this correction the systematic errors are less than 10 km s<sup>-1</sup> over the full wavelength range from 3500 Å to 10,000 Å for all galaxies.

## 4. EXTRACTED SPECTRA

The extracted spectra are shown in Fig. 5, ordered by increasing velocity dispersion. The quality is generally high: essentially all the visible features in the spectra (except in the far blue and far red) are spectral lines, not noise. Nevertheless, it is clear that some spectra have a higher S/N ratio than others. This variation largely stems from the fact that each galaxy was observed for 540 s irrespective of its brightness. The region around 9500 Å suffers from strong sky absorption (see Fig. 3a), and is shown in light grey.

For a correct interpretation of the model fits in paper II it is crucial to have realistic estimates of the noise in the spectra. The formal noise was determined from Poisson statistics, taking the gain, the sky spectrum, and the applied weighting (Eq. 1) into account. It is difficult to test whether the actual noise corresponds to the expected noise, as the observed variation in the spectra is almost entirely due to the “forest” of weak absorption lines present in the atmospheres of cool stars. We empirically determined the noise properties of the spectra in the following way. We selected two galaxies with very similar velocity dispersions, [Fe/H], and [Mg/Fe] (as determined in paper II), and an average S/N ratio which is typical for the full sample. The galaxies NGC 4570 and NGC 4660 satisfy all these criteria. A small part of their spectra, centered around the calcium triplet, is shown in Fig. 6(a). As expected from

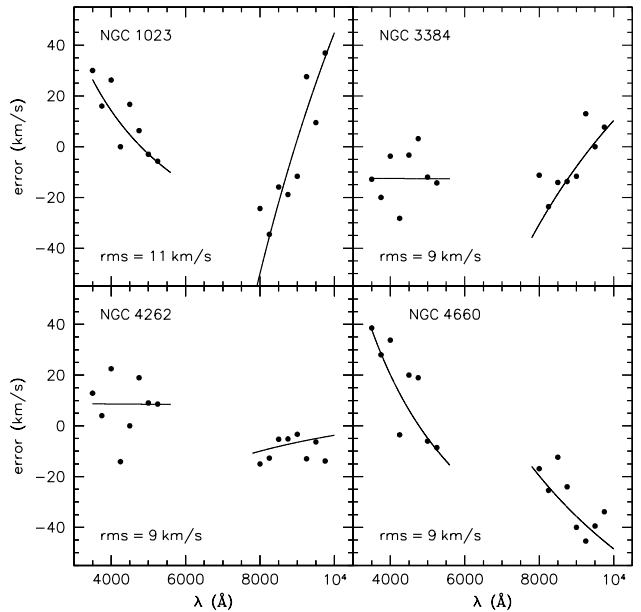


**Figure 4.** Errors in the wavelength calibration, resulting from wavelength- and time-dependent differences between the arc lamp solution and the galaxy spectra. The points were determined from model fits in 250 Å wide spectral regions; the four galaxies that are shown span the full range of variation in the errors. Lines indicate linear fits (in wavelength) to the errors; the residuals after this correction are  $\sim 10$  km s<sup>-1</sup>.

the selection the spectra are very similar, although NGC 4570 has slightly stronger absorption lines than NGC 4660.

The difference between the two normalized spectra is shown in Fig. 6b. The  $1\sigma$  scatter in the difference spectrum is  $0.0059$  Å<sup>-1</sup>, as determined with the biweight estimator (e.g., Beers, Flynn, & Gebhardt 1990). Assuming each galaxy contributes equally to the scatter this corresponds to  $\sigma \approx 0.0041$  Å<sup>-1</sup> for each individual galaxy. In Fig. 6c the scatter is calculated in bins of 20 Å and divided by the average formal error in the two spectra. A value of 1 implies that the observed differences between the spectra can be fully explained by Poisson statistics. The median is 1.1 over the displayed wavelength range and 1.2 over the entire 7800 Å – 10,200 Å range, which means that the formal errors are a good approximation of the actual uncertainties in the spectra. Similar comparisons of other galaxy pairs consistently show that the formal errors are reasonable, particularly in regions away from strong sky emission or absorption lines.

Having verified that the formal S/N ratios are reasonable, we show the S/N as a function of wavelength for all galaxies in Fig. 7. As expected there is significant variation between galaxies and between wavelengths. The S/N ratio ranges from  $\sim 60$  in the blue for the worst spectra to  $\sim 500$  in the red for the best spectra. The median S/N of all galaxies is  $90$  Å<sup>-1</sup> at 3800 Å,  $256$  Å<sup>-1</sup> at 5000 Å,  $310$  Å<sup>-1</sup> at 8500 Å, and  $211$  Å<sup>-1</sup> at 10,000 Å. There is no obvious trend with velocity dispersion.

## 5. ANALYSIS OF IMF-SENSITIVE FEATURES

Here we investigate the observed variation in the well-established IMF-sensitive features Na I  $\lambda 8183, 8195$ , the Ca II  $\lambda 8498, 8542, 8662$  triplet, and the FeH  $\lambda 9916$  Wing-Ford band. The Na I doublet and the Wing-Ford band are strong

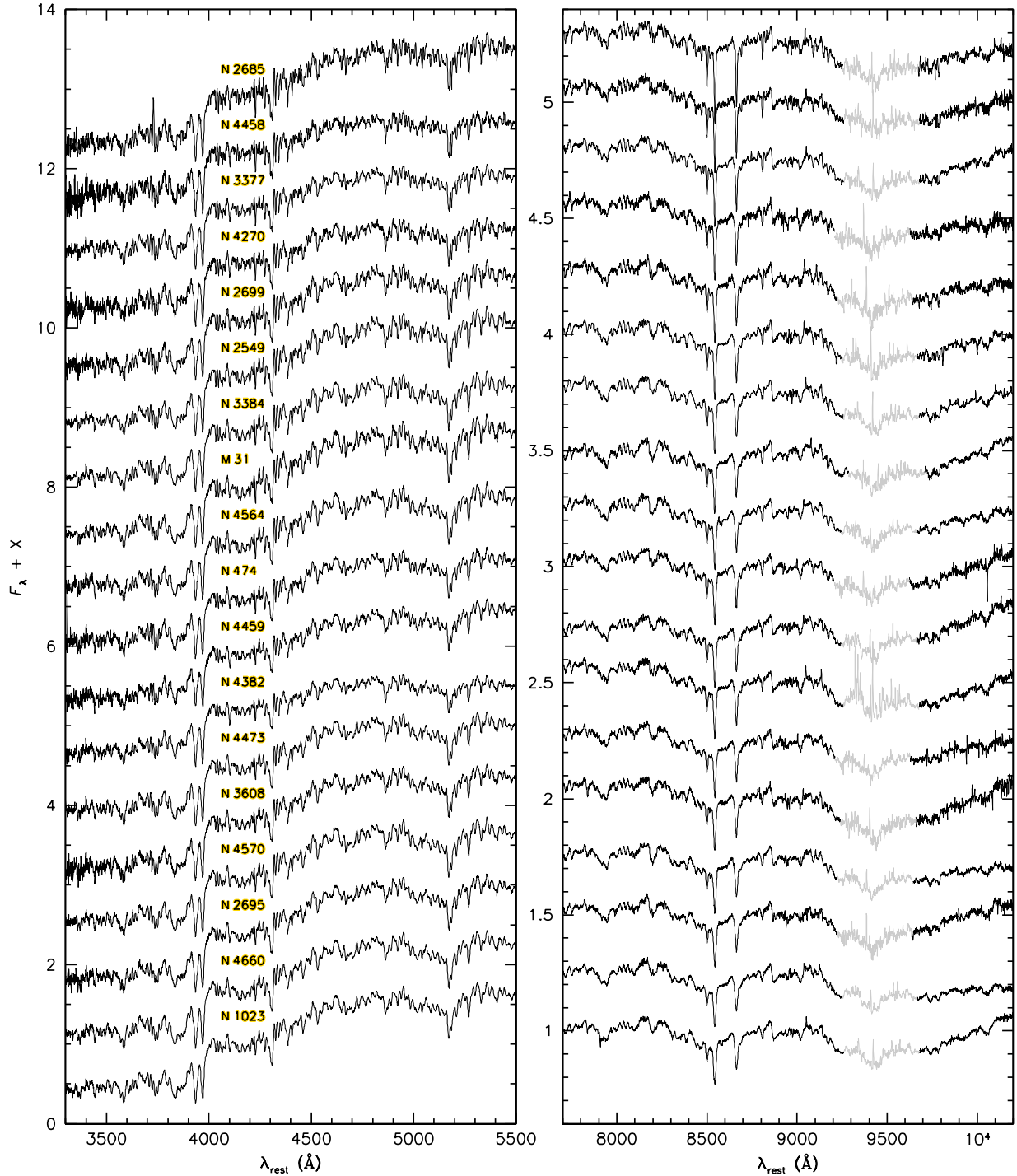


**Figure 5.** Extracted LRIS spectra in the rest-frame, using a (circularized)  $r < r_e/8$  aperture. Starting at the top galaxies are ordered by increasing velocity dispersion. The spectra are normalized at 4050 Å (blue side) and 9050 Å (red side). The region of strong sky absorption around 9500 Å is shown in light grey. The blue cutoff in the displayed red spectra is dictated by the onset of the atmospheric B band at  $\sim 7600$  Å. The spectra are of high quality, and extend beyond  $1 \mu\text{m}$  in the rest-frame.

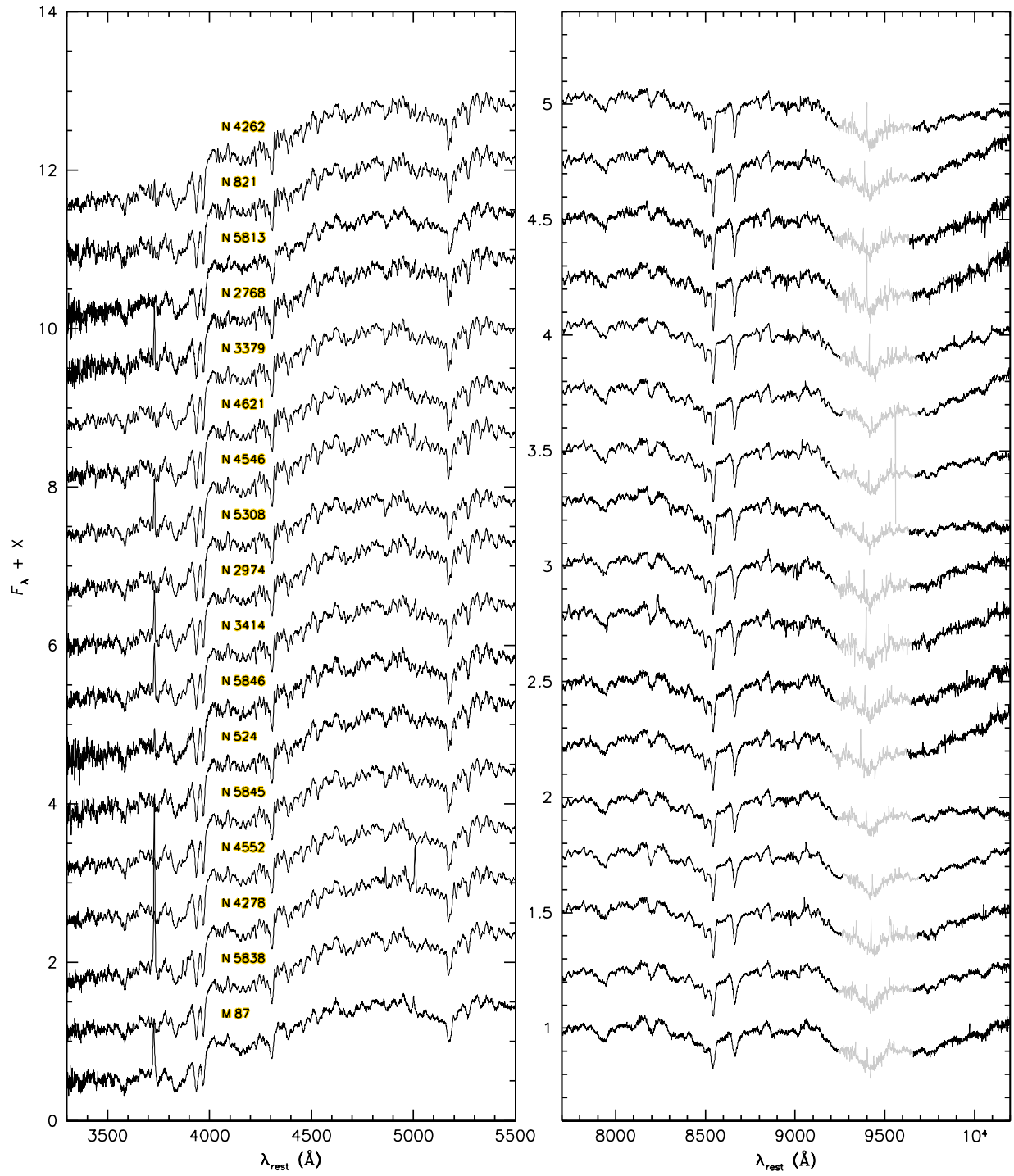
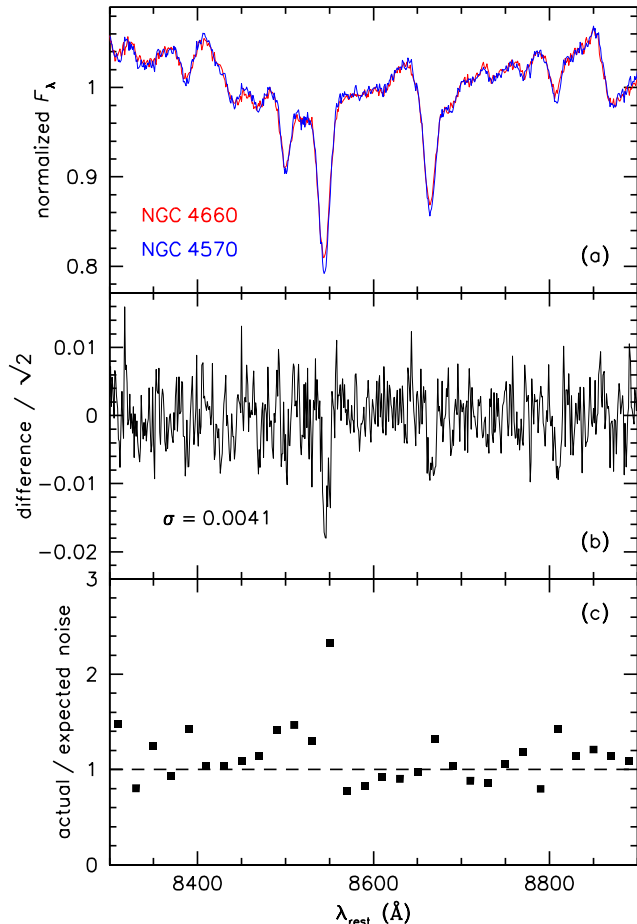


Figure 5. (continued)





**Figure 6.** (a) Comparison of the spectra of two galaxies with similar ages, abundances, and velocity dispersions, in the wavelength region near the Ca II triplet. The spectra have a S/N ratio of  $\approx 250 \text{ \AA}^{-1}$ , which is typical for our sample. (b) Difference of the two spectra. Apart from a slight difference in Ca II absorption the variation between the spectra is very small and appears mostly random. The differences (divided by  $\sqrt{2}$ ) have a 68 % range of  $\pm 0.4\%$ . (c) Observed scatter in (b) divided by the expected noise from Poisson statistics. Away from strong absorption features the observed differences between NGC 4660 and NGC 4570 are fully consistent with the formal errors. This demonstrates that the formal errors are a good approximation of the uncertainties in the spectra.

in dwarf stars and weak in giants; conversely, the Ca II triplet is strong in giants and weak in dwarfs. As a result, galaxies with bottom-heavy IMFs are expected to have stronger Na I, stronger Wing-Ford, and weaker Ca II absorption than galaxies with bottom-light IMFs (see Couture & Hardy 1993; Cenarro et al. 2003; van Dokkum & Conroy 2010; Conroy & van Dokkum 2012, and many other studies).

### 5.1. Dispersion Matching

Prior to measuring the strength of absorption lines the galaxies have to be smoothed to the same velocity dispersion. Velocity dispersions of the individual galaxies were measured directly from the extracted spectra, taking the instrumental resolution and the resolution of the template into account (see paper II). All galaxies except M87 were smoothed to a common resolution, using a Gaussian of width

$$\sigma_s = \sqrt{300^2 - (\sigma_*^2 + \sigma_{\text{instr}}^2)}, \quad (3)$$

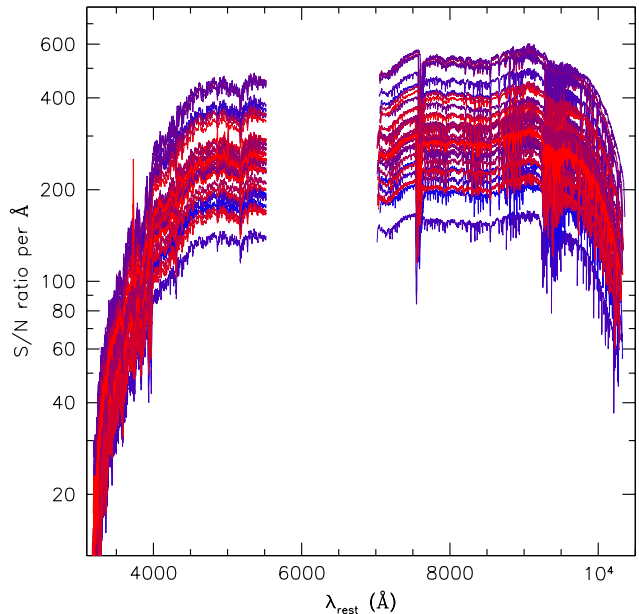


**Figure 7.** S/N ratio per rest-frame  $\text{\AA}$  for all spectra. For individual galaxies the S/N is fairly uniform between  $\sim 4500 \text{ \AA}$  and  $\sim 10,000 \text{ \AA}$ , but there is considerable variation between galaxies. The spectra are color-coded according to their velocity dispersion, from low = blue to high = red. There is no strong correlation between S/N ratio and velocity dispersion.

with  $\sigma_*$  the stellar velocity dispersion and  $\sigma_{\text{instr}}$  the instrumental resolution. This smoothing has the potential to broaden localized sky line residuals, thus “contaminating” the spectrum on 300 km/s scales. To prevent this, and to reduce the effect of sky line residuals on measured absorption line indices, pixels coinciding with strong sky lines were not taken into account in the smoothing. This was done iteratively, in each iteration replacing pixels in the unsmoothed spectrum that coincide with sky lines by pixels from the smoothed spectrum of the previous iteration.

### 5.2. Na I, the Wing-Ford band, and Ca II

The three IMF sensitive absorption lines are detected with high significance in all galaxies, as shown in Fig. 8. The top panels show the spectra at their original spectral resolution; in the bottom panels they are smoothed to a common velocity dispersion of  $300 \text{ km s}^{-1}$ . For clarity only one line of the calcium triplet is shown. The spectra were divided by a linear fit to the side-bands of the features (see below). The bulge of M31 and M87 are not shown; NGC 3414 and NGC 3608 were also excluded because they have unexplained noise peaks in their Na I (NGC 3414) and Wing-Ford (NGC 3608) regions.

The black and yellow lines in Fig. 8 illustrate the IMF-sensitivity of these lines, using stellar population synthesis models from Conroy & van Dokkum (2012). Both models have an age of 13.5 Gyr, a Solar iron abundance, and are  $\alpha$ -enhanced with  $[\alpha/\text{Fe}] = 0.2$ . The black model is for a Chabrier (2003) IMF and the yellow model is for a bottom-heavy IMF with a logarithmic slope  $x = 3$ . The data span a similar range as these model predictions. More to the point in the context of the present paper, the data quality is sufficiently high to measure the subtle differences in absorption line strength expected from IMF variations.

As can be seen in the bottom left panel of Fig. 8 the line

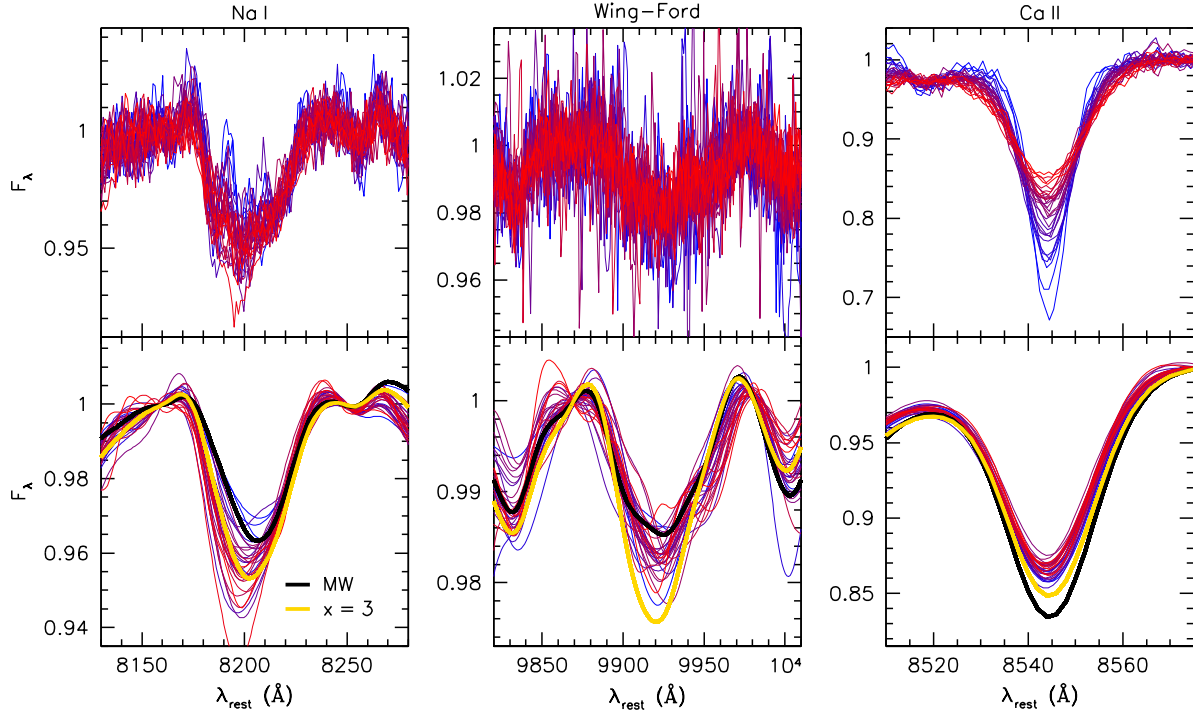


**Figure 8.** IMF-sensitive absorption features. Na I and FeH are strong in dwarf stars and weak in giants; the calcium triplet is strong in giants and weak in dwarfs. Top panels are at the original resolution; in the bottom panels the spectra are smoothed to a common dispersion of  $300 \text{ km s}^{-1}$ . The spectra are color-coded by their velocity dispersion, going from blue (low) to red (high). The black and yellow lines show expectations for 13.5 Gyr old,  $\alpha$ -enhanced stellar populations with two different IMFs (Milky Way and bottom-heavy). The dispersion-matched spectra have sufficiently high S/N ratio to distinguish between these predictions.

profile of the observed Na I feature changes with its depth: its centroid is bluer when the absorption is stronger. We show this relation between the strength of Na I and its centroid (here simply defined as the wavelength of maximum absorption) explicitly in Fig. 9. The relation arises because Na I is a blend of the Na I  $\lambda\lambda 8183, 8195$  doublet and the TiO (0,2) bandhead at a resolution of  $300 \text{ km s}^{-1}$  (see Schiavon et al. 1997a). As the sodium absorption becomes stronger the centroid of the feature shifts toward the Na I doublet and away from the TiO bandhead. This effect is illustrated in the inset of Fig. 9, which shows the effect of increasing the number of dwarf stars (and hence the sodium doublet strength) on the measured feature at  $300 \text{ km s}^{-1}$  resolution. The existence of the tight relation in Fig. 9 demonstrates that the observed variation in the Na I feature strength is driven by variation in Na I absorption, not variation in the TiO band.

The relation between centroid and feature strength also provides an empirical upper limit to the errors in the line strength measurements. Excluding the two most deviant points, we find that the centroid of the feature predicts its strength with an rms scatter of only 0.0033 (dashed line in Fig. 9). This is a strict upper limit on the error as errors in the centroid measurements, variations in the TiO bandhead, and variation in other absorption features in the central band or side bands all contribute to this scatter. The tight relation has another interesting implication. As will be shown in paper II the form of the IMF correlates with the Na I strength. Therefore one could, in principle, infer the IMF from a simple, model-independent measurement: the centroid of the Na I feature at a resolution of  $300 \text{ km s}^{-1}$ .

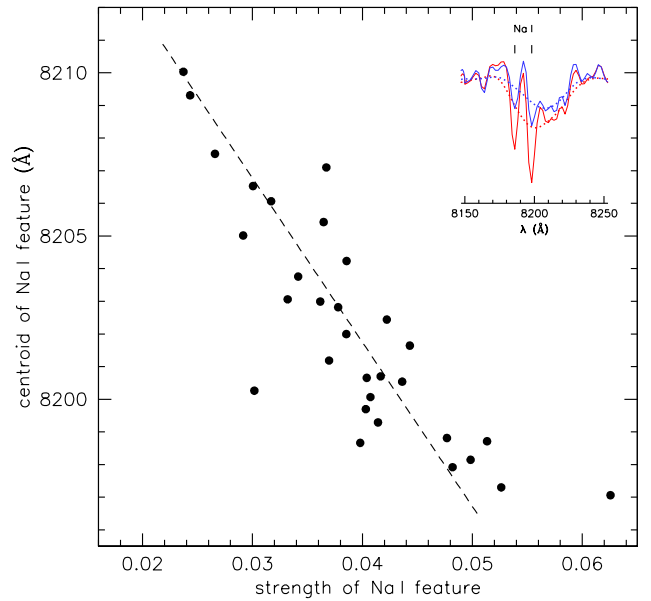


**Figure 9.** Correlation between the centroid of the Na I feature and its strength. The inset shows the origin of the correlation. The blue line is for a bottom-light IMF with weak Na I absorption and the red line is for a bottom-heavy IMF with strong Na I absorption. The broken lines show the same spectra at  $300 \text{ km s}^{-1}$  resolution. At this resolution the doublet is blended with a TiO bandhead at  $\sim 8205 \text{ \AA}$ , and increased Na I absorption moves the centroid of the measured absorption feature toward that of the bluer Na I doublet.

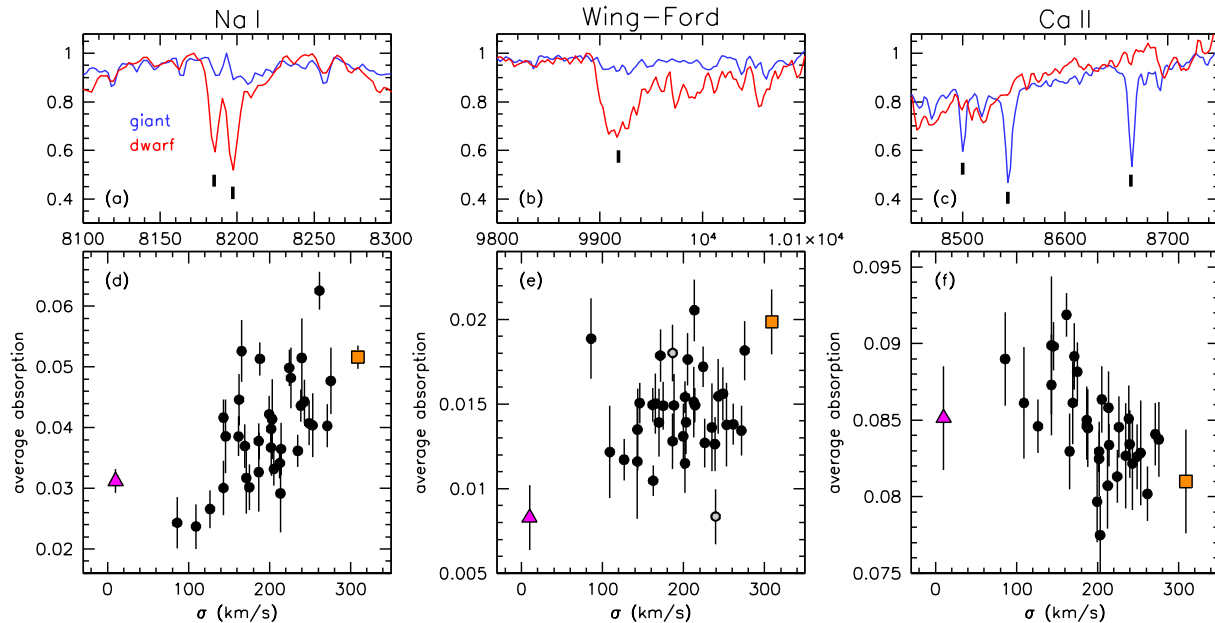


**Figure 10.** (a-c): The Na I doublet, the Wing-Ford band, and the Ca II triplet in the M6 dwarf Gliese 406 (red) and the M4 giant HD 4408 (blue). For a larger dwarf-to-giant ratio Na I and Wing-Ford are expected to be stronger and Ca II is expected to be weaker. (d-f): The strength of these features in integrated light, as a function of velocity dispersion. Black dots are individual SAURON galaxies. The purple triangle represents metal-rich globular clusters in M31 (van Dokkum & Conroy 2011), and the orange square is measured from the average spectrum of high-dispersion elliptical galaxies in the Virgo cluster (van Dokkum & Conroy 2010). Na I and Ca II show strong and opposing trends, consistent with more bottom-heavy IMFs for galaxies with higher dispersions. The relation between the Wing-Ford band and  $\sigma$  is only significant when the globular clusters and the massive Virgo galaxies are included.

### 5.3. Correlations With Velocity Dispersion

The spectra in Fig. 8 are color-coded by their velocity dispersion. In the top panels the dispersion is trivially related to the width of the feature; this is particularly obvious for the calcium line in the top right panel. In the bottom panels the spectra are smoothed to the same dispersion, and yet trends with the galaxies' velocity dispersion remain: galaxies with high velocity dispersions tend to show strong Na I absorption and weak Ca II triplet absorption.

We analyze these trends by measuring the absorption line strengths of the IMF-sensitive features. Such line strengths are useful for highlighting trends of specific absorption features in the data. However, we note here that line indices are notoriously difficult to interpret quantitatively as they rarely measure the abundance of a single element in a straightforward way. Their central bands or side bands typically contain faint lines of other elements (e.g., Schiavon et al. 1997a; Kelson et al. 2006); they suffer from well-documented degeneracies between age and abundance (e.g., Worthey 1994); and multiple features of the same element are typically needed to differentiate abundance effects from IMF effects (Conroy & van Dokkum 2012). For these reasons we do not use line indices in paper II, where we quantify the IMF, but fit the galaxy spectra directly with comprehensive stellar population synthesis models.

The relation between the strength of IMF sensitive features and velocity dispersion is shown in Fig. 10. The line strengths are defined as the average absorption over a central band, with the continuum determined by interpolating between two side bands. The errorbars are a combination of the formal Poisson uncertainty (which dominates for the Wing-Ford band and Ca II) and the uncertainty introduced by the atmospheric absorption correction (which dominates for Na I). For Na I and

the Wing-Ford band we use the same central and side band definitions as in van Dokkum & Conroy (2010). For Ca II we use the definitions of Conroy & van Dokkum (2012). Also shown are measurements from stacked spectra of metal-rich globular clusters in M31 from van Dokkum & Conroy (2011) and of high velocity dispersion elliptical galaxies in the Virgo cluster from van Dokkum & Conroy (2010).

The strength of the two dwarf-sensitive features (Na I and the Wing-Ford band) systematically increases with velocity dispersion. M31 globular clusters have the weakest absorption, the four Virgo ellipticals from van Dokkum & Conroy (2010) have the strongest absorption, and the SAURON galaxies fall in between. By contrast, the strength of the giant-sensitive Ca II triplet *decreases* with velocity dispersion, as was found earlier by Cenarro et al. (2003). These trends are consistent with a systematically increasing dwarf contribution with  $\sigma$ . We note, however, that the Wing-Ford band does not show a significant correlation with  $\sigma$  within the SAURON sample (i.e., disregarding the globular clusters and the most massive ellipticals). The correlation coefficient is positive (0.12) but not significant. By contrast, the probability that the (anti-)correlations of Na I and Ca II with  $\sigma$  are caused by chance are 0.3% and 0.1% respectively.

The trends within the SAURON sample are graphically illustrated in Fig. 11, which shows the variation in the galaxy spectra ordered by velocity dispersion. It is remarkable that the IMF-sensitive Na I and Ca II features show the strongest variation of any lines in the red. Figure 11 also highlights the well-known fact that many other spectral features show systematic trends with  $\sigma$ : most notably the Balmer lines and the [OIII] emission lines, but also Mg  $\lambda$ 5270 and a host of other metal lines (see, e.g., Trager et al. 2000b, and many other studies).

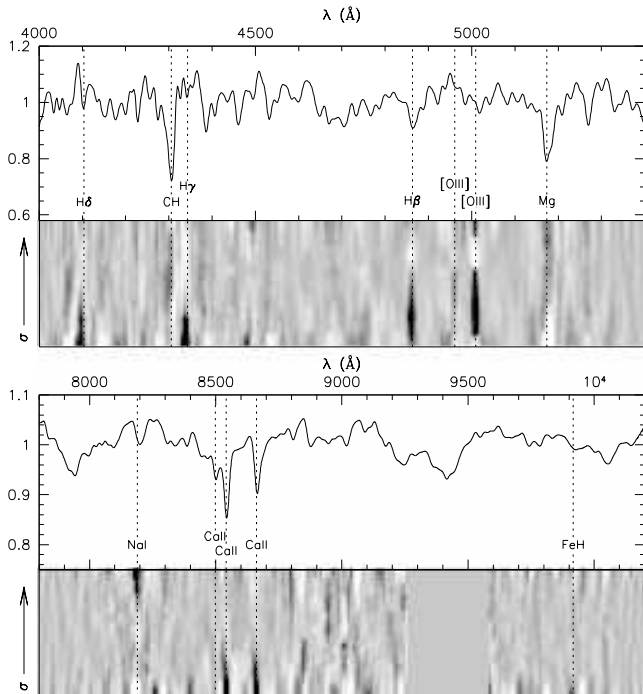


**Figure 11.** Variation in the spectra of the SAURON galaxies. The top panels show the average de-redshifted spectrum of all sample galaxies, smoothed to a common velocity dispersion of  $300 \text{ km s}^{-1}$  and divided by a 5th order polynomial. The greyscale shows the differences between individual galaxy spectra and this averaged spectrum, after smoothing and median filtering. For clarity the variation in the red is increased by a factor of three compared to the variation in the blue. Of all spectral lines at  $\lambda > 7800 \text{ \AA}$  the IMF-sensitive Na I and Ca II features show the strongest trends with  $\sigma$ .

## 6. SUMMARY AND CONCLUSIONS

In this paper we presented deep spectroscopy of a sample of early-type galaxies in the nearby Universe, obtained with LRIS on Keck I. The spectra are weighted in such a way that they are representative for a circular aperture of radius  $r = r_e/8$ . Owing to the fully depleted LBNL detectors in the red arm of LRIS the S/N ratio of the spectra is high all the way to  $\sim 1 \mu\text{m}$ . The high S/N ratio and the absence of fringing make it possible to measure absorption lines with  $< 0.5\%$  uncertainty in the far red. The reduced spectra are available upon request.

The analysis in the present paper is limited to a relatively qualitative assessment of IMF-sensitive spectral features in the red part of the spectra. The Na I  $\lambda 8183, 8195$  doublet and the FeH  $\lambda 9916$  Wing-Ford band are strong in dwarfs and weak in giants, whereas the Ca II  $\lambda 8498, 8542, 8662$  triplet is weak in dwarfs and strong in giants. We find that all three features show considerable variation within the sample. Na I and the Wing-Ford band vary by a factor of  $\sim 2$ . When abundance and age variations are ignored, this variation directly translates into a variation of a factor of  $\sim 2$  in the number of low mass stars. Ca II varies only by  $\sim 10\%$ , but this is expected as

giants dominate the light. As part of the analysis we demonstrate that the variation in the Na I feature is indeed due to variation in the strength of the Na I doublet and not driven by the neighboring TiO bandhead (see, e.g., Schiavon et al. 1997a, for a discussion of this issue).<sup>4</sup>

The variation in IMF-sensitive features correlates with the velocity dispersion of the galaxies: a higher velocity dispersion implies stronger Na I, a stronger Wing-Ford band, and weaker Ca II. The anti-correlation of Ca II and velocity dispersion was previously discussed by Cenarro et al. (2003), who also interpreted it as a possible IMF effect. These results extend our earlier measurements of very massive ellipticals in the Virgo cluster (van Dokkum & Conroy 2010) and metal-rich globular clusters in M31 (van Dokkum & Conroy 2011); these previous studies “bookend” the SAURON galaxies at very high and very low dispersions respectively.

As shown in Conroy & van Dokkum (2012) it is hazardous to derive quantitative IMF constraints from these three features alone, as age and abundance variations contribute to the observed absorption line strengths. The Wing-Ford band is sensitive to the Fe abundance, Na I is sensitive to  $[\text{Na}/\text{Fe}]$ , and the Ca II triplet is very sensitive to  $[\text{Ca}/\text{Fe}]$  (and the overall  $\alpha$ -enhancement). All three indices also depend on age, in complex ways (see, e.g., Fig. 12 in Conroy & van Dokkum 2012a). In our initial paper on the most massive galaxies in Virgo and Coma we mostly ignored these effects, which was perhaps justified because the IMF effects were so strong in that sample. However, it is clear that the trends in Fig. 10 to some extent reflect the correlations of age and metal line abundances with velocity dispersion (see, e.g., Trager et al. 2000a; Thomas et al. 2005; Kelson et al. 2006; Sánchez-Blázquez et al. 2006; Graves, Faber, & Schiavon 2009; Scott et al. 2009; Worthey, Ingermann, & Serven 2011, and many other studies).

In a companion paper (Conroy & van Dokkum 2012b) we use a comprehensive stellar population synthesis model to quantify the IMF variation among the early-type galaxies discussed in the present paper. This model allows for abundance variations of individual elements, which is critical as it removes the ad-hoc assumption that we understand relative elemental abundances better than we understand the IMF. Furthermore, we fit the entire spectrum of each galaxy rather than line indices, which means that blended spectral lines are treated correctly.

The data presented herein were obtained at the W. M. Keck Observatory, which is operated as a scientific partnership among the California Institute of Technology, the University of California and the National Aeronautics and Space Administration. The Observatory was made possible by the generous financial support of the W. M. Keck Foundation. The authors wish to recognize and acknowledge the very significant cultural role and reverence that the summit of Mauna Kea has always had within the indigenous Hawaiian community. We are most fortunate to have the opportunity to conduct observations from this mountain.

<sup>4</sup> Although we can resolve this particular issue, the Na I ambiguity illustrates the difficulty of interpreting line indices: essentially all indices reflect

a canopy of blended spectral lines.

APPENDIX  
COMPARISON TO VAN DOKKUM (2008)

Building on many previous studies of the fundamental plane (e.g., Djorgovski & Davis 1987; van der Wel et al. 2004; van Dokkum & van der Marel 2007) and the color-magnitude relation (e.g., Bower, Lucey, & Ellis 1992a; Stanford, Eisenhardt, & Dickinson 1998; Holden et al. 2004), van Dokkum (2008) [vD08] constrained the slope of the IMF near  $1 M_{\odot}$  in early-type galaxies by comparing their luminosity evolution to their color evolution. This test, first proposed by Tinsley (1980), is based on the expectation that luminosity and color evolution depend on the IMF in different ways. As discussed in Tinsley (1980) and in § 2.1 of vD08 a more bottom-heavy IMF should lead to slower luminosity evolution and faster color evolution. Therefore, a comparison of luminosity evolution to color evolution of a sample of galaxies should provide strong constraints on the slope of the IMF near the main sequence turn-off ( $\approx 1 M_{\odot}$ ).

The application of this test to massive early-type galaxies in clusters at  $0 < z < 1$  yielded a surprising result: the slow rest-frame  $U-V$  color evolution of the galaxies and fast evolution of their rest-frame  $M/L_B$  ratios seemed to imply an IMF that is deficient in low mass stars (“bottom-light”) compared to the IMF in the Milky Way. The key result from vD08 is shown in Fig. A1a. The green line is the predicted evolution of a Maraston (2005) model with super-Solar metallicity ( $[Z/H]=0.35$ ) and a Salpeter IMF. This model is not a good fit to the data: the green line has a slope  $a = \Delta \log(M/L_B) / \Delta(U-V) = 1.5$ , whereas a fit to the data gives  $a = 2.6$ . From Eq. 5 and 6 in vD08 it follows that the slope of the IMF near  $1 M_{\odot}$  is in the range  $0.1 \lesssim x \lesssim 1.3$  depending on the metallicity, where  $x = 2.3$  is the value for both a Milky Way IMF and a Salpeter IMF.<sup>5</sup>

This finding is in apparent conflict with the results in van Dokkum & Conroy (2010, 2011) and paper II. Contradictory results are not exactly uncommon in this particular field (examples can be found in the review by Bastian, Covey, & Meyer 2010). However, in this case the contradiction is rather extreme (bottom-light versus bottom-heavy with respect to the Milky Way) and applies to the exact same galaxies (massive early-type galaxies in clusters).<sup>6</sup> Note that the results of vD08 are *not* in conflict with recent mass measurements of early-type galaxies (Treu et al. 2010; Cappellari et al. 2012; Spiniello et al. 2012), as a bottom-light IMF and a bottom-heavy IMF can result in very similar  $M/L$  ratios.<sup>7</sup>

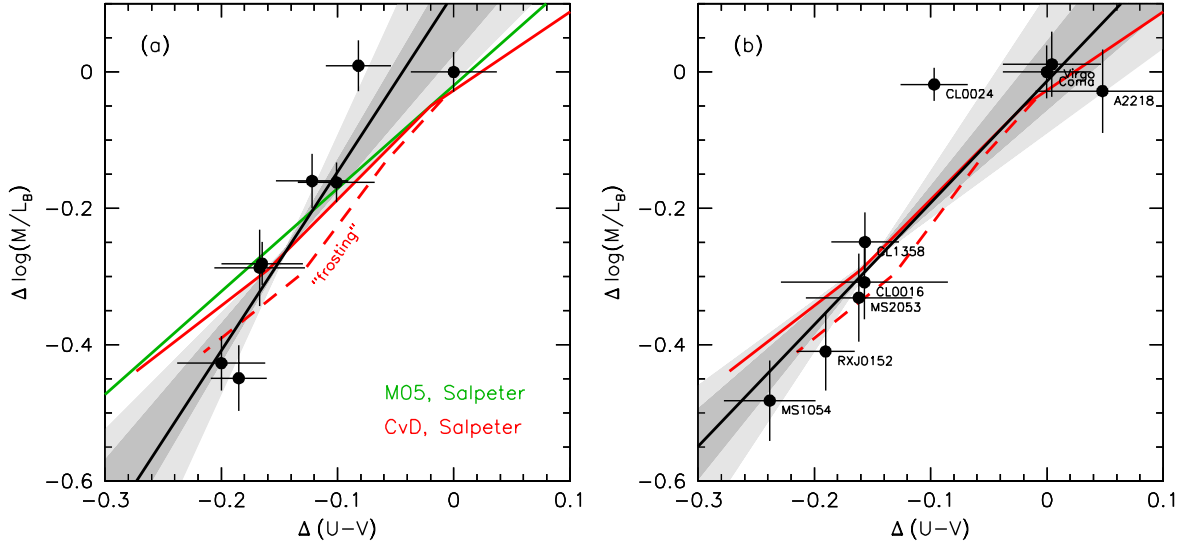


**Figure A1.** Color and luminosity evolution of early-type galaxies in clusters. (a) Evolution at fixed dynamical mass, for galaxies with  $M > 10^{11} M_{\odot}$ . This panel is nearly identical to Fig. 5 in van Dokkum (2008); the only difference is that no corrections for progenitor bias were applied. Lines show expectations for a Salpeter (1955) IMF, for a high metallicity Maraston (2005) model with  $[Z/H]=0.35$  (green) and for an  $\alpha$ -enhanced Conroy & van Dokkum (2012a) model with  $[Fe/H]=0$  and  $[\alpha/Fe]=0.2$  (red). The black line is the best fit to the data; grey regions indicate the 68 % and 95 % confidence limits of the best-fitting slope. The models predict lower luminosity evolution at fixed color evolution than observed, although a CvD model with “frosting” of young stars comes close to the data. (b) Evolution at fixed velocity dispersion, for galaxies with  $\sigma > 200 \text{ km s}^{-1}$ , and including the Virgo cluster. The CvD models are a satisfactory fit to the data.

Here we update the data and models of vD08 and examine whether they can be brought into agreement with the absorption line studies that indicate heavy mass functions. Compared to the analysis in vD08 the following changes were made:

1. The  $[Z/H]=0.35$  Maraston (2005) model was replaced by an  $[Fe/H]=0$ ,  $[\alpha/Fe]=0.2$  Conroy & van Dokkum (2012) [CvD] model. As shown in Fig. A1 the  $M/L$  ratio in the CvD model evolves slightly faster in the age range 5–9 Gyr, although the

<sup>5</sup> Note that in vD08 the IMF was defined such that the Salpeter form corresponds to a slope of 1.35.

<sup>6</sup> For those readers who failed to notice this: the 2008 and 2010 studies also have the same first author. <sup>†</sup>

<sup>†</sup> This is not a coincidence: the 2010 paper was partly motivated by the

desire to confirm <sup>‡</sup> the conclusions of the 2008 paper using a more direct method.

<sup>‡</sup> This did not work out quite as expected.

<sup>7</sup> For a bottom-light IMF the “extra” mass is not in the form of low mass stars but is comprised of the remnants of high mass stars (white dwarfs, neutron stars, and black holes).

difference is small. It remains true that stellar population synthesis models are in reasonable agreement on the evolution of rest-frame optical colors and luminosities.

2. A model with mild “frosting” of young stars was created (dashed line in Fig. A1. Based on Lick indices Trager, Faber, & Dressler (2008) finds that early-type galaxies in the Coma cluster have relatively young absolute luminosity-weighted ages, similar to early-type galaxies in the general field. A possible explanation is that early-type galaxies have a small fraction of relatively young stars in addition to a dominant old population (see, e.g., Trager et al. 2000a). The dashed line is for a model in which 80 % of the stars have ages between 3 and 13.5 Gyr and 20 % of the stars are 3 Gyr old.
3. In vD08 there was only one nearby cluster, Coma, for which both accurate  $U - V$  colors and  $M/L$  ratio measurements were available. We added the Virgo cluster to have another datapoint in the  $\Delta \log(M/L_B) \sim \Delta(U - V) \sim 0$  region of Fig. A1. Effective radii and surface brightnesses were obtained from Burstein et al. (1987). The effective radii are in excellent agreement with the data in Cappellari et al. (2006). Surface brightnesses were corrected from the average surface brightness within  $r_e$  to the surface brightness at  $r_e$  and corrected for cosmological surface brightness dimming. A distance of 16.5 Mpc was assumed, based on surface brightness fluctuations measured in the ACS Virgo Cluster Survey (Mei et al. 2007). Velocity dispersions were obtained from Davies et al. (1987), multiplied by 0.95 to undo the aperture correction, and then corrected to a  $3''/4$  diameter circular aperture at the distance of Coma (see Jørgensen, Franx, & Kjærgaard 1995). The  $U - V$  colors were obtained from Bower, Lucey, & Ellis (1992b).
4. A key assumption in vD08 was that structural evolution of the galaxies could be ignored. As discussed in Holden et al. (2010) this assumption is important: the measured color and luminosity evolution can be different from the true evolution if the masses and sizes of the galaxies change with time. Following earlier results for field galaxies (e.g., Daddi et al. 2005; Trujillo et al. 2006; van Dokkum et al. 2008) there is now evidence for size evolution in clusters, such that cluster galaxies of a given mass were smaller at higher redshifts (van der Wel et al. 2008; Strazzullo et al. 2010; Raichoor et al. 2012). Whether this applies to all clusters is still unclear, as is the question whether the size evolution is driven by infall from the field or changes to individual cluster galaxies (e.g., van der Wel et al. 2009). However, it does suggest that structural evolution needs to be considered. To address this issue Holden et al. (2010) measured the color- and  $M/L$  evolution of early-type galaxies at fixed velocity dispersion rather than mass, reasoning that the velocity dispersion is probably a more stable parameter (see, e.g., Bezanson et al. 2011). From a comparison of the Coma cluster to a single cluster at  $z = 0.83$  they found that the color and  $M/L$  evolution of galaxies at fixed dispersion is only  $2.3\sigma$  removed from expectations of a Salpeter IMF. We now follow Holden et al. (2010) and measure offsets in color and  $M/L$  ratio from the  $U - V - \sigma$  and  $M/L_B - \sigma$  relations,<sup>8</sup> for galaxies with  $\sigma > 200 \text{ km s}^{-1}$ .

The results of these updates are shown in Fig. A1b. The data are now in much better agreement with a Salpeter IMF. The best-fitting relation has a slope of  $a = 1.81 \pm 0.27$ , which means that the high-metallicity Maraston (2005) model with a Salpeter IMF is only  $1.2\sigma$  removed from the data. The Conroy & van Dokkum (2012) model is in even better agreement, particularly if some frosting is included. We infer that the luminosity and color evolution of massive early-type galaxies does not rule out IMFs with Salper-like slopes near  $\sim 1 M_\odot$ , contrary to the conclusions of vD08.

<sup>8</sup> Note that in calculating  $M/L$  ratios we are still assuming that homology is conserved, which is almost certainly incorrect; see, for instance, van Dokkum

et al. (2010) and Buitrago et al. (2011).

## REFERENCES

- Auger, M. W., Treu, T., Gavazzi, R., Bolton, A. S., Koopmans, L. V. E., & Marshall, P. J. 2010, *ApJ*, 721, L163
- Bacon, R., Copin, Y., Monnet, G., Miller, B. W., Allington-Smith, J. R., Bureau, M., Carollo, C. M., Davies, R. L., et al. 2001, *MNRAS*, 326, 23
- Bastian, N., Covey, K. R., & Meyer, M. R. 2010, *ARA&A*, 48, 339
- Bate, M. R., Bonnell, I. A., & Bromm, V. 2003, *MNRAS*, 339, 577
- Beers, T. C., Flynn, K., & Gebhardt, K. 1990, *AJ*, 100, 32
- Bezanson, R., van Dokkum, P. G., Franx, M., Brammer, G. B., Brinchmann, J., Kriek, M., Labbé, I., Quadri, R. F., et al. 2011, *ApJ*, 737, L31+
- Bohlin, R. C. 1996, *AJ*, 111, 1743
- Bower, R. G., Lucey, J. R., & Ellis, R. S. 1992a, *MNRAS*, 254, 601
- . 1992b, *MNRAS*, 254, 589
- Buitrago, F., Trujillo, I., Conselice, C. J., & Haeussler, B. 2011, *ArXiv e-prints*
- Burstein, D., Davies, R. L., Dressler, A., Faber, S. M., Stone, R. P. S., Lynden-Bell, D., Terlevich, R. J., & Wegner, G. 1987, *ApJS*, 64, 601
- Cappellari, M., Bacon, R., Bureau, M., Damen, M. C., Davies, R. L., de Zeeuw, P. T., Emsellem, E., Falcón-Barroso, J., et al. 2006, *MNRAS*, 366, 1126
- Cappellari, M., McDermid, R. M., Alatalo, K., Blitz, L., Bois, M., Bournaud, F., Bureau, M., Crocker, A. F., et al. 2012, *ArXiv e-prints*
- Carter, D., Visvanathan, N., & Pickles, A. J. 1986, *ApJ*, 311, 637
- Cenarro, A. J., Gorgas, J., Vazdekis, A., Cardiel, N., & Peletier, R. F. 2003, *MNRAS*, 339, L12
- Chabrier, G. 2003, *PASP*, 115, 763
- Cohen, J. G. 1978, *ApJ*, 221, 788
- Conroy, C. & van Dokkum, P. 2012, *ApJ*, 747, 69
- Couture, J. & Hardy, E. 1993, *ApJ*, 406, 142
- Daddi, E., Renzini, A., Pirzkal, N., Cimatti, A., Malhotra, S., Stiavelli, M., Xu, C., Pasquali, A., et al. 2005, *ApJ*, 626, 680
- Davé, R. 2008, *MNRAS*, 385, 147
- Davies, R. L., Burstein, D., Dressler, A., Faber, S. M., Lynden-Bell, D., Terlevich, R. J., & Wegner, G. 1987, *ApJS*, 64, 581
- de Zeeuw, P. T., Bureau, M., Emsellem, E., Bacon, R., Carollo, C. M., Copin, Y., Davies, R. L., Kuntschner, H., et al. 2002, *MNRAS*, 329, 513
- Djorgovski, S. & Davis, M. 1987, *ApJ*, 313, 59
- Dutton, A. A., Mendel, J. T., & Simard, L. 2012, *MNRAS*, 422, L33
- Emsellem, E., Cappellari, M., Krajnović, D., van de Ven, G., Bacon, R., Bureau, M., Davies, R. L., de Zeeuw, P. T., et al. 2007, *MNRAS*, 379, 401
- Faber, S. M. & French, H. B. 1980, *ApJ*, 235, 405
- Fardal, M. A., Katz, N., Weinberg, D. H., & Davé, R. 2007, *MNRAS*, 379, 985
- Graves, G. J., Faber, S. M., & Schiavon, R. P. 2009, *ApJ*, 698, 1590
- Holden, B. P., Stanford, S. A., Eisenhardt, P., & Dickinson, M. 2004, *AJ*, 127, 2484
- Holden, B. P., van der Wel, A., Kelson, D. D., Franx, M., & Illingworth, G. D. 2010, *ApJ*, 724, 714
- Hopkins, P. F., Hernquist, L., Cox, T. J., Keres, D., & Wuyts, S. 2009, *ApJ*, 691, 1424
- Jørgensen, I., Franx, M., & Kjaergaard, P. 1995, *MNRAS*, 276, 1341
- Kelson, D. D., Illingworth, G. D., Franx, M., & van Dokkum, P. G. 2006, *ApJ*, 653, 159
- Kormendy, J., Fisher, D. B., Cornell, M. E., & Bender, R. 2009, *ApJS*, 182, 216
- Kriek, M., van Dokkum, P. G., Franx, M., Illingworth, G. D., Marchesini, D., Quadri, R., Rudnick, G., Taylor, E. N., et al. 2008, *ApJ*, 677, 219
- Kroupa, P. 2001, *MNRAS*, 322, 231
- Krumholz, M. R. 2011, *ApJ*, 743, 110
- Kuntschner, H., Emsellem, E., Bacon, R., Cappellari, M., Davies, R. L., de Zeeuw, P. T., Falcón-Barroso, J., Krajnović, D., et al. 2010, *MNRAS*, 408, 97
- Larson, R. B. 2005, *MNRAS*, 359, 211
- Maraston, C. 2005, *MNRAS*, 362, 799
- Mei, S., Blakeslee, J. P., Côté, P., Tonry, J. L., West, M. J., Ferrarese, L., Jordán, A., Peng, E. W., et al. 2007, *ApJ*, 655, 144
- Myers, A. T., Krumholz, M. R., Klein, R. I., & McKee, C. F. 2011, *ApJ*, 735, 49
- Naab, T., Johansson, P. H., Ostriker, J. P., & Efstathiou, G. 2007, *ApJ*, 658, 710
- Oke, J. B., . . . & ETAL. 1995, *PASP*, 107, 375
- Oser, L., Ostriker, J. P., Naab, T., Johansson, P. H., & Burkert, A. 2010, *ApJ*, 725, 2312
- Padoan, P. & Nordlund, Å. 2002, *ApJ*, 576, 870
- Raichoor, A., Mei, S., Stanford, S. A., Holden, B. P., Nakata, F., Rosati, P., Shankar, F., Tanaka, M., et al. 2012, *ApJ*, 745, 130
- Rockosi, C., Stover, R., Kibrick, R., Lockwood, C., Peck, M., Cowley, D., Bolte, M., Adkins, S., et al. 2010, in *Society of Photo-Optical Instrumentation Engineers (SPIE) Conference Series*, Vol. 7735, *Society of Photo-Optical Instrumentation Engineers (SPIE) Conference Series*
- Salpeter, E. E. 1955, *ApJ*, 121, 161
- Sánchez-Blázquez, P., Gorgas, J., Cardiel, N., & González, J. J. 2006, *A&A*, 457, 787
- Schiavon, R. P. 1998, PhD thesis, Universidade de São Paulo, Brazil (1998)
- Schiavon, R. P., Barbuy, B., Rossi, S. C. F., & Milone, A. 1997a, *ApJ*, 479, 902
- Schiavon, R. P., Barbuy, B., & Singh, P. D. 1997b, *ApJ*, 484, 499
- Scott, N., Cappellari, M., Davies, R. L., Bacon, R., de Zeeuw, P. T., Emsellem, E., Falcón-Barroso, J., Krajnović, D., et al. 2009, *MNRAS*, 398, 1835
- Spiniello, C., Koopmans, L. V. E., Trager, S. C., Czoske, O., & Treu, T. 2011, *MNRAS*, 417, 3000
- Spiniello, C., Trager, S. C., Koopmans, L. V. E., & Chen, Y. 2012, *ArXiv e-prints*
- Spinrad, H. 1962, *ApJ*, 135, 715
- Spinrad, H. & Taylor, B. J. 1971, *ApJS*, 22, 445
- Stanford, S. A., Eisenhardt, P. R., & Dickinson, M. 1998, *ApJ*, 492, 461
- Strazzullo, V., Rosati, P., Pannella, M., Gobat, R., Santos, J. S., Nonino, M., Demarco, R., Lidman, C., et al. 2010, *A&A*, 524, A17
- Thomas, D., Maraston, C., Bender, R., & Mendes de Oliveira, C. 2005, *ApJ*, 621, 673
- Thomas, J., Saglia, R. P., Bender, R., Thomas, D., Gebhardt, K., Magorrian, J., Corsini, E. M., Wegner, G., et al. 2011, *MNRAS*, 415, 545
- Tinsley, B. M. 1980, *Fundamentals of Cosmic Physics*, 5, 287
- Trager, S. C., Faber, S. M., & Dressler, A. 2008, *MNRAS*, 386, 715
- Trager, S. C., Faber, S. M., Worthey, G., & González, J. J. 2000a, *AJ*, 120, 165
- Trager, S. C., Faber, S. M., Worthey, G., & González, J. J. 2000b, *AJ*, 119, 1645
- Treu, T., Auger, M. W., Koopmans, L. V. E., Gavazzi, R., Marshall, P. J., & Bolton, A. S. 2010, *ApJ*, 709, 1195
- Trujillo, I., Förster Schreiber, N. M., Rudnick, G., Barden, M., Franx, M., Rix, H.-W., Caldwell, J. A. R., McIntosh, D. H., et al. 2006, *ApJ*, 650, 18
- van der Wel, A., Bell, E. F., van den Bosch, F. C., Gallazzi, A., & Rix, H.-W. 2009, *ApJ*, 698, 1232
- van der Wel, A., Franx, M., van Dokkum, P. G., & Rix, H.-W. 2004, *ApJ*, 601, L5
- van der Wel, A., Holden, B. P., Zirm, A. W., Franx, M., Rettura, A., Illingworth, G. D., & Ford, H. C. 2008, *ApJ*, 688, 48
- van Dokkum, P. G. 2008, *ApJ*, 674, 29
- van Dokkum, P. G. & Conroy, C. 2010, *Nature*, 468, 940
- . 2011, *ApJ*, 735, L13
- van Dokkum, P. G., Franx, M., Kriek, M., Holden, B., Illingworth, G. D., Magee, D., Bouwens, R., Marchesini, D., et al. 2008, *ApJ*, 677, L5
- van Dokkum, P. G. & van der Marel, R. P. 2007, *ApJ*, 655, 30
- van Dokkum, P. G., Whitaker, K. E., Brammer, G., Franx, M., Kriek, M., Labbé, I., Marchesini, D., Quadri, R., et al. 2010, *ApJ*, 709, 1018
- Wilkins, S. M., Trentham, N., & Hopkins, A. M. 2008, *MNRAS*, 385, 687
- Wing, R. F. & Ford, Jr., W. K. 1969, *PASP*, 81, 527
- Worthey, G. 1994, *ApJS*, 95, 107
- Worthey, G., Ingermann, B. A., & Serven, J. 2011, *ApJ*, 729, 148